



Crystallization of a Zr-based metallic glass produced by laser powder bed fusion and suction casting

A. Ericsson^{a,*}, V. Pacheco^b, J.J. Marattukalam^c, R.M. Dalgliesh^d, A.R. Rennie^e, M. Fisk^{a,f}, M. Sahlberg^b

^a Division of Solid Mechanics, Lund University, PO Box 118, Lund, SE 22100, Sweden

^b Department of Chemistry, Ångström Laboratory, Uppsala University, Box 523, Uppsala, SE 75120, Sweden

^c Department of Physics & Astronomy, Materials Physics, Uppsala University, Box 516, Uppsala, SE 75121, Sweden

^d ISIS Pulsed Neutron and Muon Source, Science and Technology Facilities Council, Rutherford Appleton Laboratory, Harwell Science and Innovation Campus, Didcot OX11 0QX, UK

^e Centre for Neutron Scattering, Uppsala University, Box 516, Uppsala, SE 75121, Sweden

^f Materials Science and Applied Mathematics, Malmö University, Malmö, SE 20506, Sweden

ARTICLE INFO

Keywords:

AMZ4
Additive manufacturing
Small angle scattering
Crystallization
Oxygen

ABSTRACT

The crystallization behaviour during low temperature annealing of samples of the $Zr_{59.3}Cu_{28.8}Al_{10.4}Nb_{1.5}$ (at%) bulk metallic glass produced by suction casting and the laser powder bed fusion (LPBF) process were studied with small angle neutron scattering (SANS), X-ray diffraction and scanning electron microscopy. The *in-situ* SANS measurements during isothermal annealing reveals that the phase separation in the LPBF processed material proceeds at a smaller characteristic length-scale than the cast material. Quantitative analysis of the SANS data shows that, while the crystallization process in both materials proceed through rapid nucleation followed by diffusion limited growth, the LPBF processed material crystallizes with a smaller cluster size and at a higher rate. The smaller cluster size is attributed to the elevated oxygen content in the LPBF processed material which reduces the nucleation barrier and thus the thermal stability.

1. Introduction

Bulk metallic glasses (BMG) are alloys with an amorphous atomic structure, which are typically obtained by cooling sufficiently fast to bypass crystallization. The amorphous structure possess a unique combination of material properties such as high specific strength, high elastic strain limit, high mechanical resilience, improved corrosion resistance and tunable magnetic properties [1], which make these materials suitable for a wide range of engineering applications, such as spring materials, structural components and precision tools [1,2].

Laser powder bed fusion (LPBF) is a promising processing technique for the fabrication of BMGs. The localized melting and solidification of powder material allows for high cooling rates (10^3 – 10^8 K s⁻¹) [3,4], which enables the possibility of producing BMG components larger than the critical casting thickness [5,6]. So far, Fe-, Zr-, Ti- and Al-based glass-forming alloys have been successfully produced by LPBF [5,7–9]. Recent studies have focused on the influence of the periodic laser processing on porosity, structural and chemical heterogeneity,

crystallization, and mechanical properties of the fabricated components [4,6,9–15]. Despite the high cooling rates, the localised laser processing leads to cyclic heating and cooling which causes crystallization at high laser energy densities [3,4,9,10]. This imposes limitations on the processing window, since high laser energy densities are required for fusion of the powder and thus low porosity of the final product [3,9,10]. Hence, an increased understanding of the crystallization process in LPBF processing of BMGs is of considerable interest in the development towards dense and amorphous components.

Studies of crystallization in BMGs are typically performed on laboratory grade material made from high purity elements. Industrial grade metals are less expensive but contains a higher amount of impurities, especially oxygen. The role of oxygen is of particular importance as it is known to deteriorate the glass forming ability of Zr-based glasses [16, 17], causing the glass to crystallize as oxygen-induced compounds [18–21]. Depending on the alloy composition and the oxygen content, different phases may form. At low oxygen contents (<0.8%), the formation of oxygen enriched quasicrystals have been reported for multiple

* Corresponding author.

E-mail address: anders.ericsson@solid.lth.se (A. Ericsson).

<https://doi.org/10.1016/j.jnoncrysol.2021.120891>

Received 26 February 2021; Received in revised form 16 April 2021; Accepted 23 April 2021

Available online 11 August 2021

0022-3093/© 2021 The Authors. Published by Elsevier B.V. This is an open access article under the CC BY license (<http://creativecommons.org/licenses/by/4.0/>).

Zr-based alloys [18,19,21], while at elevated oxygen contents, the big-cube NiZr_2 -type phase (space group $\text{Fd}\bar{3}\text{m}$) may form [20,21]. Oxygen enriched crystals, notably the big-cube NiZr_2 -type phase, has been found in LPBF processing of different Zr-based BMGs [11,14,22].

In terms of the LPBF process, oxygen is especially difficult to handle. The high surface to volume ratio of the powder feedstock material enables Zr-based materials to react with oxygen to form thin oxide layers on the outer surface, which can dissolve into the material when melted. Another issue is control of the atmosphere in the LPBF process [22]. Zr-based alloys can readily dissolve oxygen in the molten state and increased oxygen contents in LPBF processed laboratory pure Zr-based BMGs have been reported [11,15].

In the present work, the crystallization of LPBF processed and suction cast AMZ4 ($\text{Zr}_{59.3}\text{Cu}_{28.8}\text{Al}_{10.4}\text{Nb}_{1.5}$ (at%)) [23], an industrially available bulk metallic glass, is studied during low temperature annealing. The characteristics of the nucleation process is investigated using *in-situ* small angle neutron scattering (SANS), *ex-situ* X-ray diffraction (XRD) and scanning electron microscopy (SEM). The results are analysed and discussed in terms of the different manufacturing routes.

2. Materials and experimental methods

Samples of AMZ4, $\text{Zr}_{59.3}\text{Cu}_{28.8}\text{Al}_{10.4}\text{Nb}_{1.5}$ (at%), were produced using LPBF and suction casting. The feedstock material for the LPBF process was supplied by Heraeus Additive Manufacturing GmbH [24]. Note that during the time of this study, Heraeus adopted the trade name AMLOY-ZR01 for alloy AMZ4. The powder was produced by vacuum inert gas atomization, resulting in spherical particles subsequently sieved to a size distribution between 10 and 45 μm . Rectangular plates with length, width and thickness of 22 mm, 11 mm and 2 mm, respectively, were manufactured using an EOS M100 (200 W, Yb-fiber laser), with a laser power of 75 W, laser spot diameter of 40 μm , scan speed of 2 m s^{-1} , hatch spacing of 100 μm and a layer thickness of 20 μm under an argon gas flow. A remelting scan strategy (each layer melted twice) with 67° rotations between each layer was employed. The process parameters have been developed to minimize crystallization and porosity in the as-printed part, for further details see [9].

The suction cast samples of AMZ4 were produced by Heraeus Additive Manufacturing GmbH. High purity elements (>99.9%) were used to produce ingots of a master alloy by electric arc melting synthesis. The master alloy was remelted and cast in a water cooled copper mold into 5 mm cylindrical rods, which were cut to rectangular plates with length, width and thickness of 22 mm, 5 mm and 2 mm, respectively, for the SANS measurements. The arc-melting and suction casting were performed in a Ti-gettered, high purity, argon atmosphere.

The oxygen content of the powder feedstock material, the LPBF produced and cast material was determined using the inert gas fusion method at Laboratory Testing Inc., USA. The samples were fused in a graphite crucible with a high purity inert gas at a temperature of 3000 °C. The initial oxygen content of the samples were determined based on measurements of CO and CO₂, which is the product of the reaction between the material and the crucible.

2.1. In-situ small angle neutron scattering

In-situ small angle neutron scattering measurements were performed using the Larmor instrument at the ISIS Pulsed Neutron and Muon Facility. The prepared specimens were measured using a beam size of 8 × 8 mm for the printed material and 3 × 10 mm for the cast material. The material was placed in the center of an infrared radiation furnace connected to a PID controller coupled with a thermocouple in contact with the sample [25]. Two cast and two LPBF samples were annealed for up to ten hours at 350 °C and two hours at 370 °C under a flow of nitrogen gas. Background scattering was determined with measurement of the furnace with no sample present. The wavelength dependent transmission of each

sample was measured before and after heat treatment with a detector in the direct beam. Each raw scattering data set was corrected for the detector efficiencies, sample transmission and background scattering and converted to differential scattering cross-section data ($\partial\Sigma/\partial\Omega$ vs q) using the Mantid framework [26]. Here, the momentum transfer q is defined as $q = 4\pi\sin(\theta)/\lambda$, where 2θ is the scattering angle and λ is the wavelength. Data in the q range of 0.0047 to 0.4778 \AA^{-1} were then placed on an absolute intensity scale (cm^{-1}) using the scattering from a reference sample (a solid blend of hydrogenous and perdeuterated polystyrene) [27]. The data were recorded using event-mode and subsequently sliced into parts using the Mantid software. To capture the transient behaviour, the time slices were chosen to vary with annealing time and the following integration intervals were used: 15 min (0–2 h), 30 min (2–4 h) and 1 h (4–10 h). The data are reported at the midpoint of each time interval and the differential scattering cross-section is hereafter denoted as $I(q)$.

2.2. Ex-situ X-ray diffraction and electron microscopy

The annealed samples were examined *ex-situ* using X-ray diffraction and scanning electron microscopy. The XRD measurements were performed using a Bruker D8 Advance Diffractometer operating at 40 kV and 40 mA with $\text{CuK}\alpha$ radiation and Bragg-Brentano experimental geometry. The SEM images were taken at an accelerating voltage of 20 kV with a Zeiss LEO1550 system equipped with a backscattered electron detector and in-lens detector at a working distance of 8.5 mm. The samples were polished with a SiC paper and then with a SiO₂ suspension prior to the study.

3. Results and discussions

In the following, the various results are presented. The measured oxygen levels of the samples are presented in Section 3.1. In Section 3.2, the results from the characterization using XRD and SEM are presented, followed by the results from the SANS measurements in Section 3.3.

3.1. Oxygen content of samples

The measured oxygen content of the powder material, LPBF processed and cast samples are presented in Table 1. Both the powder material and the cast material were processed using high purity elements, however, the oxygen content of the powder material is significantly higher as a result of the atomization process. The elevated oxygen content of the powder material translates into a comparable weight fraction of oxygen in the LPBF processed material and only a slight increase in oxygen result from the LPBF process.

3.2. Characterization of annealed samples

The microstructure and crystallography of the annealed cast and LPBF samples were studied with XRD and SEM. The XRD pattern of the LPBF processed sample annealed at 370 °C is shown in Fig. 1 where distinct crystalline peaks are present. Similar XRD patterns were observed for all samples. The peaks are indexed as CuZr_2 and Al_3Zr_4 phases, which have been confirmed to form as stable phases during continuous heating of both LPBF processed and cast AMZ4 [14]. In the study by Pacheco et al. [14], the oxygen enriched $\text{Cu}_2\text{Zr}_4\text{O}$ phase (NiZr_2 -type, $\text{Fd}\bar{3}\text{m}$) formed in the LPBF processed material during the initial stages of the heating process. At later times and elevated

Table 1

Measured oxygen contents in the powder, the LPBF processed and the cast samples.

	Cast	Powder	LPBF
Oxygen (wt%)	0.02	0.20	0.23

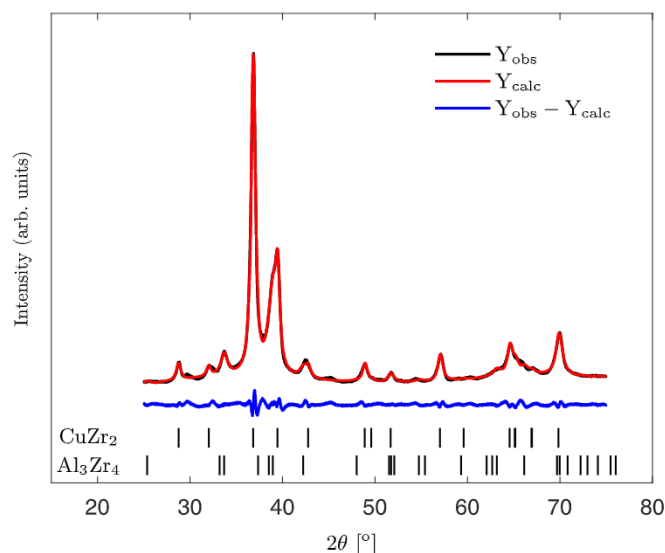


Fig. 1. XRD pattern of the LPBF processed sample annealed at 370 °C using a wavelength of $\lambda = 1.5406$ Å. Y_{obs} shows the observed data and Y_{calc} is the refined data using the Pawley method. The Bragg reflections of CuZr_2 and Al_3Zr_4 phases are shown below the intensity plots. Similar patterns were obtained for both the cast and LPBF processed samples as shown in Fig. S1. The magnitude of intensity is shown in Fig. S2. The unit cell parameters obtained from the Pawley refinement are presented in Table S3.

temperatures, the phase disappears from the XRD pattern and the material transforms to the crystalline end state, consisting of stable tetragonal CuZr_2 and hexagonal Al_3Zr_4 phases. The result is in agreement with the present study, which suggests that the CuZr_2 and Al_3Zr_4 phases are stable at low temperatures as well. The low temperature stability of the CuZr_2 and Al_3Zr_4 phases is also supported by thermodynamic modelling of the Al-Cu-Zr system [28].

Interestingly, the diffraction peaks of the $\text{Cu}_2\text{Zr}_4\text{O}$ phase could not be identified in XRD patterns. There are however, some small reflections in the diffractogram that seem to arise from an unidentified phase in small fraction. It has recently been reported that nanocrystals of the $\text{Cu}_2\text{Zr}_4\text{O}$ phase could not be detected in LPBF processed AMZ4 using a laboratory X-ray diffractometer, but was revealed by synchrotron XRD and electron microscopy [29]. The observation is in agreement with our study and the former study by Pacheco et al. [14], in which the $\text{Cu}_2\text{Zr}_4\text{O}$ phase was detected by synchrotron XRD. Considering that the formation of the $\text{Cu}_2\text{Zr}_4\text{O}$ phase is limited by the oxygen content in the material, it is probable that the phase is present in a small amount. Provided that all oxygen is depleted from the matrix to form crystals, the volume fraction of the $\text{Cu}_2\text{Zr}_4\text{O}$ phase would be 2% at most, which is likely below the detection limit of the laboratory X-ray diffractometer [30]. The above calculation is based on the measured oxygen content in Table 1 and the composition profile of $\text{Cu}_2\text{Zr}_4\text{O}$ crystals in LPBF processed AMZ4 [9]. Hence, the nucleation and growth of $\text{Cu}_2\text{Zr}_4\text{O}$ crystals should become saturated at extended annealing times as the crystallization process proceeds through the formation of CuZr_2 and Al_3Zr_4 phases. Indeed, it has been proposed that the formation of oxygen enriched crystals in Zr-based BMGs serve as heterogeneous nucleation sites for further crystallization [1,31], which is in line with our observations and would further explain why the $\text{Cu}_2\text{Zr}_4\text{O}$ phase is absent in the diffraction pattern of the annealed LPBF samples.

The formation of crystalline phases during annealing is further confirmed by examination of the SEM images of the LPBF and cast samples in Figs. 2 and 4, respectively. The images show a large population density of nano-sized crystalline particles embedded in a matrix. While the cast samples show a homogeneous distribution of particles, the crystallization appears to be more localized in the LPBF samples, forming dense banded regions of nanocrystals. Fig. 3 shows a magnified

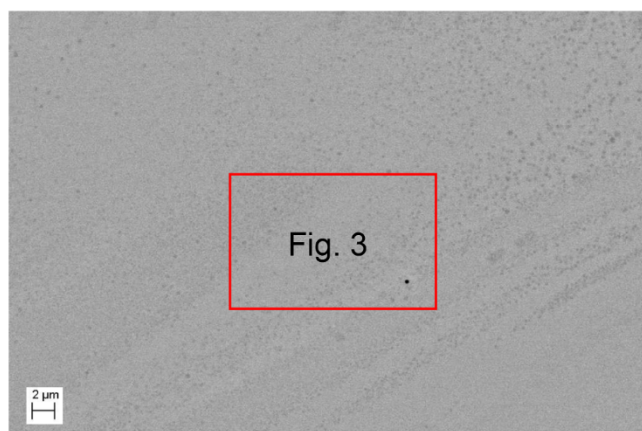


Fig. 2. Backscattered SEM image of LPBF sample annealed at 350 °C. Crystals are shown by the gray particles. A magnified image of the inset is shown in Fig. 3.

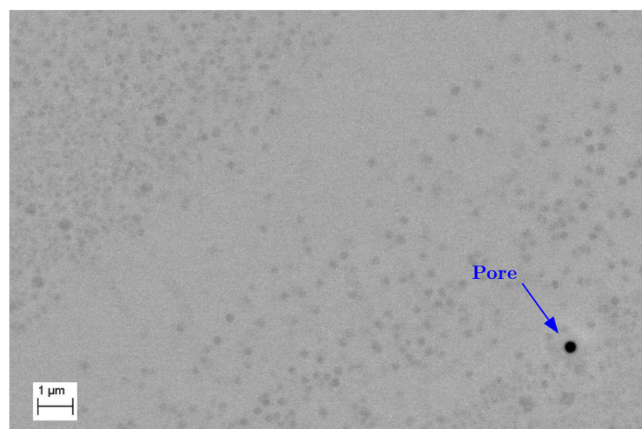


Fig. 3. A magnified image of the inset in Fig. 2, showing the localized variations in crystal size and number density.

image of the interface between the regions, in which a variation of crystal density and size is clearly visible. In the banded regions, the crystals appear to be of smaller sizes, while in the areas with lower cluster density, the crystals are of larger size. The formation of banded crystalline regions in the LPBF processed samples is possibly a result of the localized thermal processing. Variations in thermal history and

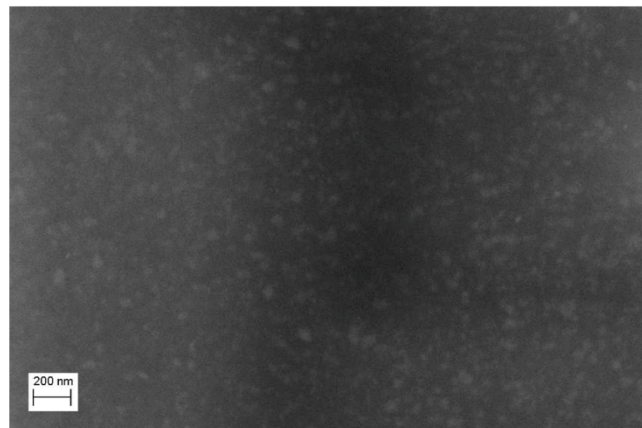


Fig. 4. In-lens SEM image of cast sample annealed at 370 °C. The light particles are crystals. The particles are more homogeneously distributed than in the LPBF samples.

temperature gradient, as well as the influence of melt pool convection can cause structural and chemical heterogeneity in the fused amorphous material [10,12,32]. Such phenomena could locally change the conditions favouring nucleation and growth that results in local variations in number density and particle size upon annealing.

3.3. Small angle neutron scattering during annealing

Figs. 5(a) and 6(a) shows the evolution of the scattering of the cast and LPBF processed samples during annealing at 350 °C and 370 °C, respectively (typical values of data uncertainty are shown in Fig. 7). The scattering of the initial state at room temperature is lower for the cast samples than for the LPBF processed samples as a result of the different processing routes as further discussed in Section 3.3.2. Overall, the scattering intensity for both the cast and the LPBF produced samples is relatively low at room temperature. The scattering at $q > 0.04 \text{ \AA}^{-1}$ is approximately uniform at an intensity of 0.01 cm^{-1} , which is lower than many materials [33]. The low scattering intensity indicates a promising potential for the material to be used as a metallic window material or sample container for neutron scattering experiments.

As time proceeds, a broad peak starts to emerge in the scattering data at $q \approx 0.03 \text{ \AA}^{-1}$ for the LPBF samples and at $q \approx 0.015 \text{ \AA}^{-1}$ for the cast samples. These evolve and shift towards lower q at longer annealing times. Similar evolution in scattering intensity has been reported in other small angle scattering studies performed on Zr-based BMGs and indicates that phase separation occurs in the material [34–39]. The scattering intensity develops faster for the samples annealed at 370 °C, which is expected due to the increased atomic mobility. The differences in peak position clearly show that the phase separation occurs at different characteristic length-scales in the LPBF and cast samples, respectively. The shift in characteristic size with time is more distinct in the Iq^2 vs q plots shown in Figs. 5(b) and 6(b), in which the peak position corresponds to a characteristic length-scale of the phase evolution.

At this point it is important to remark that different phase separation processes could give rise to the scattering peak shown in Figs. 5(b) and 6(b). Phase separation through both spinodal decomposition as well as solute partitioning associated with nucleation and growth can result in a similar scattering behaviour, consequently it is difficult to distinguish the different processes solely from the small angle scattering data [40]. For example, the scattering peak has been attributed to spinodal decomposition of the amorphous phase followed by nanocrystallization

in the decomposed Zr- and Be-rich regions during annealing of $\text{Zr}_{41.2}\text{Ti}_{13.8}\text{Cu}_{12.5}\text{Ni}_{10.0}\text{Be}_{22.5}$ known as Vit1 [34,35]. However, Martin et al. [37] carried the study further and investigated the same alloy using three-dimensional atom probe and small angle X-ray scattering (SAXS) and the evolution in small angle scattering was explained by solute partitioning associated with nanocrystalline formation. No evidence of decomposition of the amorphous phase prior to crystallization was found. Kajiwarra et al. [38] performed a similar study using three-dimensional atom probe, high-resolution electron microscopy and SAXS on $\text{Zr}_{52.5}\text{Cu}_{17.9}\text{Ni}_{14.6}\text{Al}_{10.0}\text{Ti}_{5.0}$ metallic glass, and attributed the evolution in the SAXS profile to primary crystallization of big cube NiTi_2 -type phase. Other studies on Zr-based BMGs have involved simultaneous *in-situ* XRD and SAXS measurements of low temperature crystallization, which showed that the SAXS intensity evolves approximately synchronously with the appearance of the crystalline peaks in the XRD pattern [36,39], hence the occurrence of spinodal decomposition of the amorphous phase in Zr-based BMGs prior to crystallization is questionable.

A thermodynamic requirement for spinodal decomposition of the amorphous phase is the presence of a miscibility gap in the phase diagram. In principle, depending on whether the alloying elements constitute a negative or positive enthalpy of mixing, there is a tendency towards local formation of different structure or separation into regions with preferred neighbourhood of the same atoms. With the exception of the Zr-Nb and Cu-Nb pairs, which are slightly positive, the AMZ4 alloy possess negative enthalpy of mixing between the atomic pairs as shown in Table 2, also note that Nb is dilute in the alloy. Kim et al. concluded in an extensive review on phase separation, that while it is theoretically possible for amorphous alloys with negative enthalpy of mixing to form miscibility gaps that enables spinodal decomposition in a narrow composition range, so far no clear evidence for spinodal decomposition in Zr-based BMGs with negative enthalpy of mixing has been reported [42]. Further, if such phase separation would occur, nanocrystallization would immediately follow, hence it is unlikely that the evolution of the scattering peak in Figs. 5(a) and 6(a) would arise from spinodal decomposition, especially during the late stages of the annealing process.

Considering the preceding discussion, as well as the evidence of crystallization from the XRD and SEM results in Section 3.2, the evolution of the scattering peak in Figs. 5(a) and 6(a) is attributed to nanocrystallization of the amorphous phase. Hence, a two-phase structure model of spherical particles representing the crystalline formation is

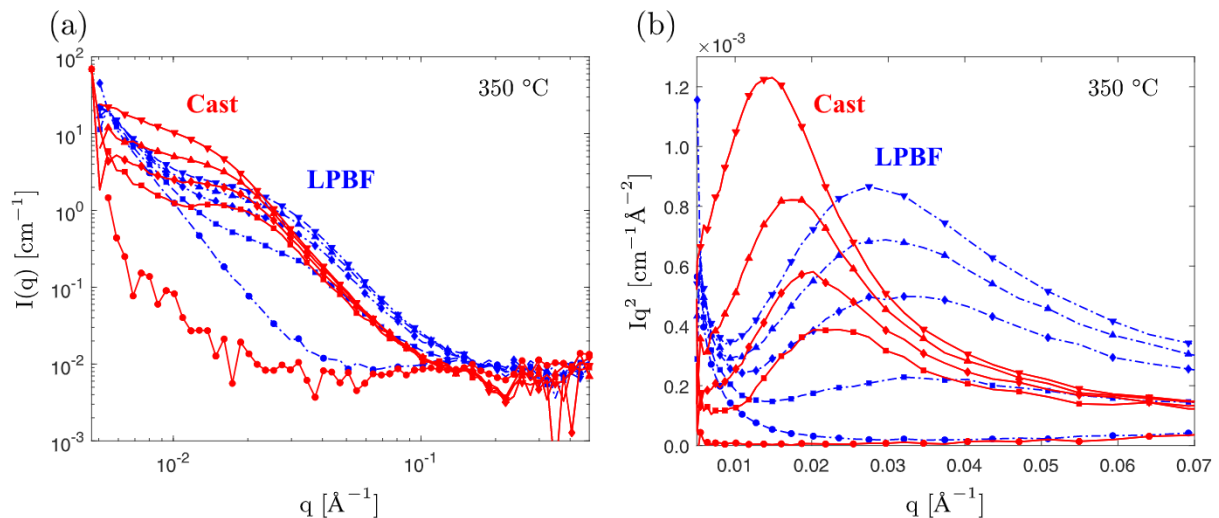


Fig. 5. (a) Differential scattering cross-section and (b) Iq^2 vs q plots for cast (solid red) and LPBF (dashed dotted blue) samples during annealing at 350 °C. The uncertainty bars have been omitted for clarity, typical values are instead shown in Fig. 7. The symbols denote the evolution in scattering: room temperature (●), 30 min (■), 90 min (◆), 205 min (▲) and 430 min (▼), the time is counted from when the samples reach 350 °C. (For interpretation of the references to color in this figure legend, the reader is referred to the web version of this article.)

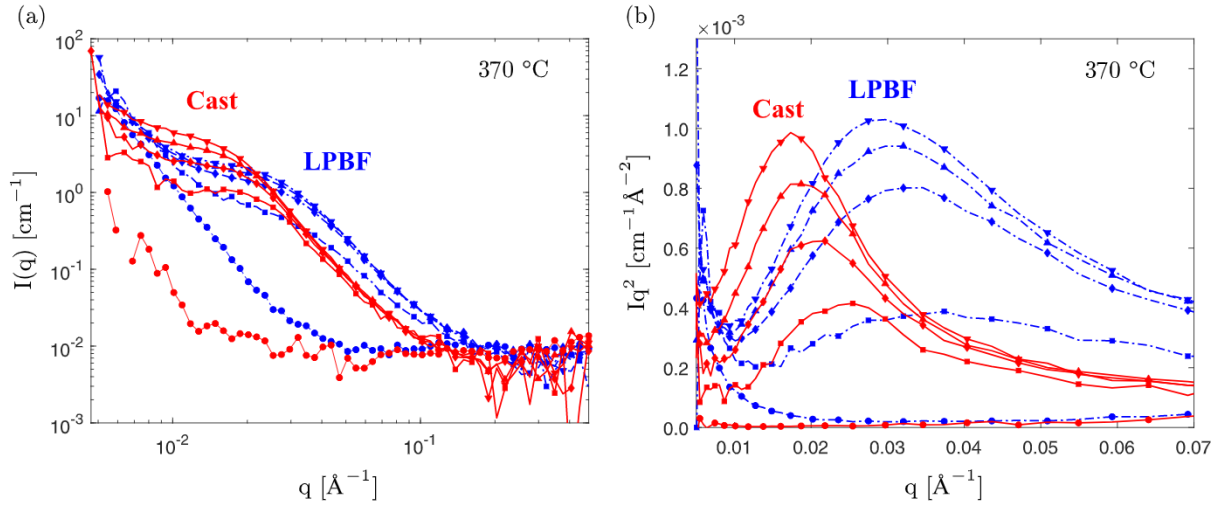


Fig. 6. (a) Differential scattering cross-section and (b) Iq^2 vs q plots for cast (solid red) and LPBF (dashed dotted blue) samples during annealing at 370 °C. The uncertainty bars have been omitted for clarity, typical values are instead shown in Fig. 7. The symbols denote the evolution in scattering: room temperature measurement (●), 0 min (■), 30 min (◆), 60 min (▲) and 90 min (▼), the time is counted from when the samples reach 370 °C. (For interpretation of the references to color in this figure legend, the reader is referred to the web version of this article.)

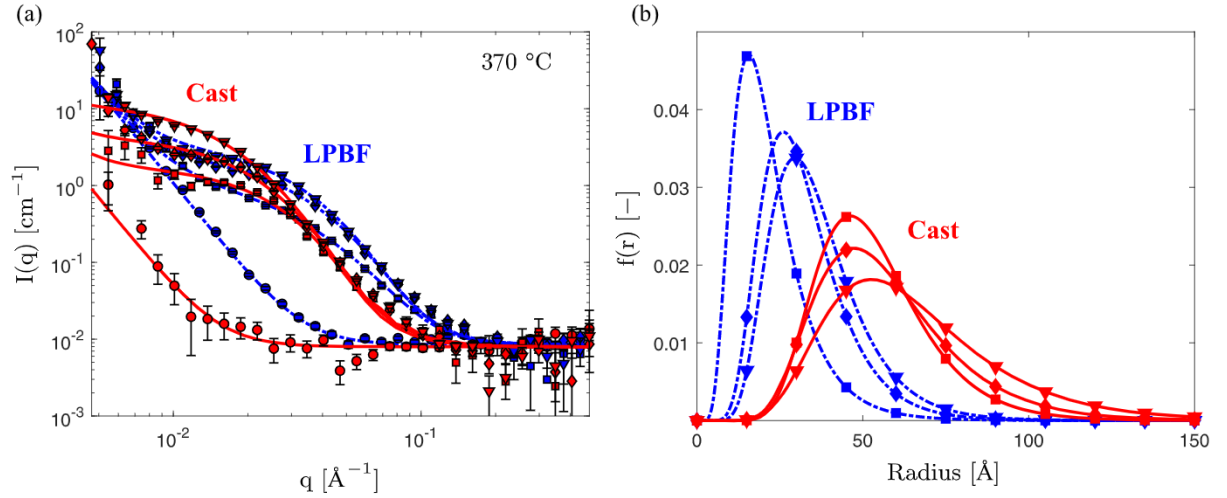


Fig. 7. (a) Differential scattering cross-section and fitted model for cast (solid red) and LPBF (dashed dotted blue) samples during annealing at 370 °C. The symbols with uncertainty bars represent the experimental data at different times and the lines are the model curves. The following data are presented: room temperature measurement (●), 0 min (■), 30 min (◆) and 90 min (▼). (b) Log-normal size distributions at the corresponding times for cast (solid red) and LPBF (dashed dotted blue) samples. The time is counted from when the samples reach 370 °C. (For interpretation of the references to color in this figure legend, the reader is referred to the web version of this article.)

Table 2

Enthalpy of mixing (ΔH_{mix} , kJ mol⁻¹) of liquid binary systems in AMZ4 [41].

Zr	Zr			
Cu	-22	Cu		
Al	-55	-10	Al	
Nb	4	3	-30	Nb

used to fit the *in-situ* SANS data in the present study.

3.3.1. Model description

Assuming a two-phase model of polydisperse spherical particles, the absolute scattering intensity is given by [43]

$$I(q) = N\Delta\rho^2 \int_0^\infty f(r, r_{med}, \sigma) \{V(r)F(q, r)\}^2 dr + c_1 q^{-\alpha} + c_0 \quad (1)$$

Table 3

Calculated scattering length densities ρ using the data from [44]. The density values are taken from [24,45]. The calculations of the Cu₂Zr₄O phase is based on energy dispersive X-ray spectroscopy measurements of particles found in LPBF produced material [9]. Here, $\Delta\rho$ is the difference in scattering length density between the amorphous matrix and the crystalline phase.

Phase	Density [g cm ⁻³]	ρ [10 ⁻⁶ Å ⁻²]	$\Delta\rho$ [10 ⁻⁶ Å ⁻²]
Amorphous (am)	6.64	3.62	-
Cu ₂ Zr ₄ O	7.29	4.32	0.70
CuZr ₂	7.04	3.80	0.18
Al ₃ Zr ₄	5.38	2.83	0.79

where N is the total number density of particles, $\Delta\rho$ is the difference in scattering length density between the particles and the matrix, $F(q, r) = 3[\sin(qr) - qr \cos(qr)]/(qr)^3$ is the amplitude of the form factor of par-

ticles with radius r and volume $V(r)$ evaluated at q . The calculated scattering length densities for the possible phases present in the material are presented in Table 3, which shows a clear difference in scattering contrast between the $\text{Cu}_2\text{Zr}_4\text{O}$ Al_3Zr_4 and the CuZr_2 and amorphous phase. Hence, it is likely that the scattering intensity arises due to separation of Al and/or O elements between the particles and the amorphous matrix. Fortunately, the $\Delta\rho$ values of $\text{Cu}_2\text{Zr}_4\text{O}$ and Al_3Zr_4 are relatively close, allowing for a comparison of the fitted parameters using a constant value of $\Delta\rho$ for fitting of the LPBF processed and cast samples.

The size distribution of particles resulting from random nucleation and growth processes can be described by a log-normal probability distribution [46]. Adopting this formulation, the normalized distribution $f(r, r_{\text{med}}, \sigma)$ of the radius for the spherical particles becomes

$$f(r, r_{\text{med}}, \sigma) = \frac{1}{\sigma r \sqrt{2\pi}} \exp\left(-\frac{1}{2\sigma^2} \ln\left(\frac{r}{r_{\text{med}}}\right)^2\right) \quad (2)$$

where r_{med} is the median particle size and σ is the width parameter of the underlying normal distribution.

The remaining two terms in Eq. (1) are included to fit the background scattering and correspond to a power law, $c_1 q^{-c_2}$, with a flat background, c_0 . For simplicity, the values of c_0 , c_1 and c_2 are obtained from fitting the background scattering at room temperature for each sample. These values were kept constant during the fitting of the data at elevated temperatures.

3.3.2. Quantitative interpretation of scattering data

The background scattering in Eq. (1) was fitted to the room temperature measurements shown in Figs. 5(a) and 6(a). The corresponding fits for the samples annealed at 370 °C are shown in Fig. 7(a). The scattering data at room temperature of the LPBF samples were successfully fitted to a value of $c_2 = -4$. The proportionality of $I \propto q^{-4}$, also known as the Porod law, suggest that the scattering intensity arises from sharp interfaces of objects larger than q_{min}^{-1} . Such interpretation could not be made with confidence for the cast samples because of the higher uncertainty in the scattering intensity at room temperature (see Fig. 7(a)). The higher intensity and the $I \propto q^{-4}$ relationship of the LPBF samples at room temperature is likely to be attributed to the porosity as a result of the LPBF process.

An estimate of the porosity can be calculated using the properties of the Porod law and an estimated value of the average pore diameter. Based on the Porod law, the surface area per unit volume A_s of the pores can be calculated using $A_s = c_1 / (2\pi(\rho_m - \rho_p)^2)$ [47], where ρ_m is the scattering length density of the amorphous matrix shown in Table 3 and ρ_p is the scattering length density of the pores, we assume this value to be zero. The value of A_s can be combined with the average pore diameter \bar{d} to form an estimate of the porosity in the LPBF samples, given by $f_p = A_s \bar{d} / 6$, where f_p is the volume fraction of pores, which are assumed to be spherical. Using the average pore diameter from optical microscopy measurements of LPBF processed AMZ4 ($\bar{d} = 7.6 \mu\text{m}$) [9], the porosity is calculated to be $f_p = 1.56 \pm 0.1\%$. The result is in agreement with porosity studies involving X-ray tomography of LPBF processed Zr-based BMGs produced using similar energy densities [3,15], suggesting that the increased scattering intensity of the LPBF samples at room temperature can mainly be attributed to the porosity resulting from the LPBF process.

The time evolution of the scattering profiles shown in Figs. 5(a) and 6(a) were fitted using the particle model. The fitted curves for the cast and LPBF samples during annealing at 370 °C are shown in Fig. 7(a). Similar curves were obtained for the samples annealed at 350 °C. The corresponding log-normal size distribution for each dataset is shown in Fig. 7(b). As the scattering peak develops and shifts to lower q , the size distribution evolves and shift to a larger particle radius and a wider size distribution, indicating nucleation, growth and possibly coarsening of nanocrystals.

Taking into consideration the results from Section 3.2, it is clear that the crystallization process involves diffusive depletion of aluminium and oxygen which may contribute to the scattering intensity. Banfi et al. showed that nucleation and diffusive depletion from a surrounding region will give rise to scattering with a peak in intensity at a q position that varies with time [40]. The change in scattering length density from the diffusion process gave rise to a core-shell model for the structure of the particles with a gradient in the shell. Core-shell particles of the $\text{Cu}_2\text{Zr}_4\text{O}$ phase have been shown to form in LPBF produced AMZ4 by transmission electron microscopy and energy dispersive X-ray spectroscopy [9]. However, the observed difference in average composition between the core and the shell was below 3 at% for each element. Such small difference in composition should not cause a significant contribution to the scattering intensity and suggest that the particle model given by Eq. (1) is a sufficient representation of the primary crystallization process in AMZ4.

Fig. 8 shows the fitted model parameters by assuming that $\Delta\rho = \rho_{\text{am}} - \rho_{\text{Al}_3\text{Zr}_4}$ is constant. This is considered a fair approximation since the estimated values of $\rho_{\text{Al}_3\text{Zr}_4}$ and $\rho_{\text{Cu}_2\text{Zr}_4\text{O}}$ are close (see Table 3). As the samples approaches the target temperature, the number density of crystals increases rapidly (0 - 40 min) followed by immediate saturation (> 40 min). The initial transient in the nucleation rate occurs concurrently with a drastic increase in radius, accompanied by a decreasing

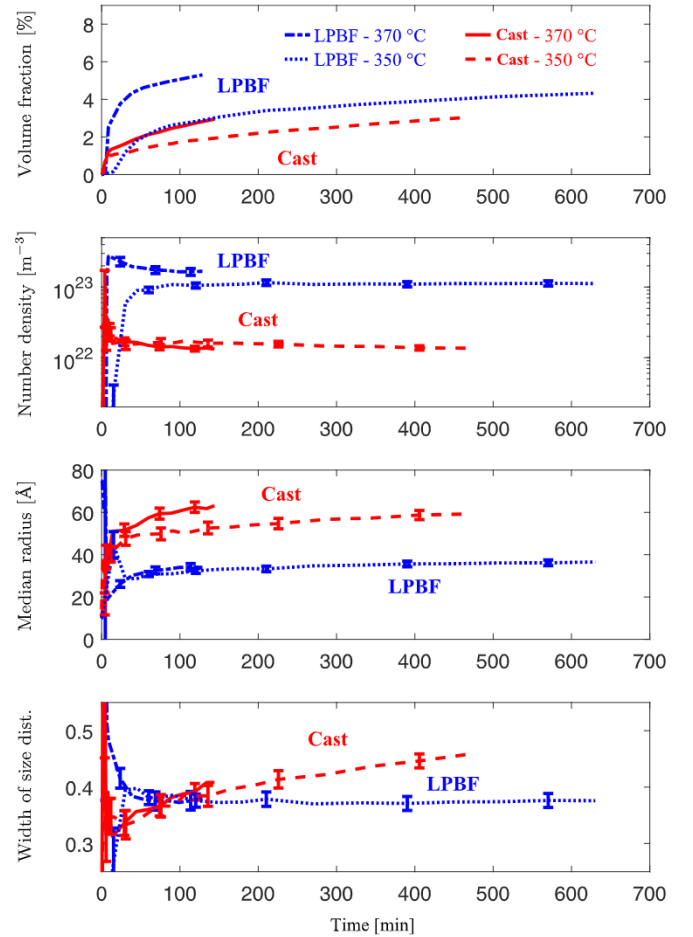


Fig. 8. The evolution (from top to bottom) of volume fraction ϕ (calculated from fitted number density and size distribution), fitted number density of particles N , median radius r_{med} and width of the size distribution σ for all samples. The particles form rapidly in the initial part of the heat treatment, followed by a declining growth rate reminiscent of diffusion limited growth. The time is shown from when the samples reach 300 °C, hence the uncertainty of the fitted parameters is initially high prior to reaching the target temperature (<10 min).

growth rate with longer annealing times. This behaviour indicates that crystallization proceeds in different stages with distinctively different transformation kinetics. In the initial stage (0 - 40 min), rapid crystallization occurs, indicative of an interface limited transformation process in which clusters form and grow by accommodating neighbouring atoms in close proximity to the clusters. As time proceeds, the material becomes saturated with nuclei competing for growth and the crystallization behaviour transitions into a diffusion limited process, in which the growth rate decreases with annealing time (> 40 min). Similar crystallization processes have been reported in SAXS studies of low temperature annealing of Zr-based BMGs [36,38,39].

The high number density of particles, apparent from the fitted parameters in Fig. 8 but also from the SEM images in Figs 2 and 4 suggest that inter-particle correlation could contribute to the total scattering intensity. To evaluate the significance of these contributions, further fitting was performed with a structure factor $S(q)$ included in the particle model in Eq. (1). The formulation of the structure factor is presented in the supplementary material and follows the "local monodisperse approximation" combined with an effective hard sphere potential [48, 49]. The fitted parameters are presented in Fig. S5 and S6. As shown, the inclusion of this empirical structure factor did not significantly affect the fitted parameters of the particle model. A larger median radius is obtained but also a wider distribution. More importantly, the radius of the hard sphere r_{hs} was fitted to be equal to the apparent radius of the particles and the effective volume fraction is high. A physical interpretation of this could be that the nanocrystals formed predominantly in regions that are separated from each other by untransformed matrix that does not contribute significantly to increased scattering. The effective volume fraction that is fitted would then correspond to a local density rather than the overall average. Since the particle model provided by Eq. (1) represents the crystallization process using fewer fitting variables, the results presented in Fig. 8 are believed to be a reasonable first approximation. The more elaborate model would be difficult to justify simply on the basis of the scattering data alone, but rationalises the observation of a non-uniform distribution of crystallites observed in the SEM images.

The evolution of the parameters in Fig. 8 suggest that the same type of crystallization process seems to occur in both the LPBF processed and cast samples, however, the fitted values of the number density and median radius are clearly different. The number density saturates at $\approx 10^{23} \text{ m}^{-3}$ for the LPBF samples and at $\approx 10^{22} \text{ m}^{-3}$ for the cast samples. These large values reflect a very high nucleation rate, which is characteristic of low temperature crystallization in Zr-based BMGs [37,50–52]. The higher nucleation rate in the LPBF samples is reflected by a smaller radius, which is approximately half of the radius of the cast samples at the same annealing temperatures. According to classical nucleation theory, the steady-state nucleation rate J_{st} under isothermal conditions can be expressed as

$$J_{st} \propto \exp\left(-\frac{W^*}{k_B T}\right) \quad (3)$$

where $W^* = 16\pi\sigma^3/(3\Delta g^2)$ is the energy of formation required to form a cluster of critical radius $r^* = 2\sigma/|\Delta g|$ [53]. The energy of formation and the critical size, and hence the nucleation rate, strongly depends on the difference in Gibbs free energy per unit volume Δg and the interfacial energy per unit area σ between the matrix and the cluster phase. While the fitted values of the median radius in Fig. 8 should not be interpreted as the critical size, the obtained large difference in size is still a strong indicator that the critical cluster size and energy of formation is smaller in the LPBF processed samples, which is likely to be a consequence of the lower thermodynamic stability caused by the elevated oxygen content.

Whether the difference in energy of formation can be attributed to changes in Gibbs free energy or interfacial energy can not be determined from the present data. However, oxygen is known to cause the formation of icosahedral quasicrystals [18,19,21], which possess a structural order

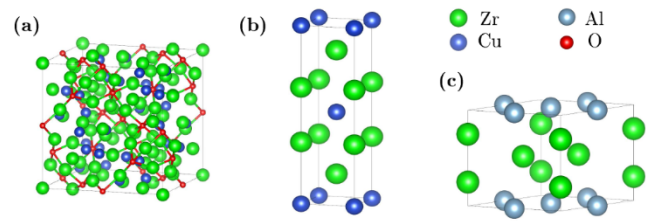


Fig. 9. Crystal structures of (a) $\text{Cu}_2\text{Zr}_4\text{O}$ phase, (b) CuZr_2 and (c) Al_3Zr_4 phases [45,57]. The large unit cell of the $\text{Cu}_2\text{Zr}_4\text{O}$ phase embodies octahedral configurations of oxygen atoms surrounded by zirconium atoms.

similar to the short-range icosahedral dominated amorphous structure. The structural compatibility between the phases result in an extremely small interfacial energy for the formation of quasicrystals [18,50,54,55]. The $\text{Cu}_2\text{Zr}_4\text{O}$ phase has a big-cube NiZr_2 -type structure, meaning that the unit cell is large and incorporates octahedral configurations in which oxygen atoms are surrounded by zirconium atoms (see Fig. 9) [20,56]. Such atomic configurations show a closer similarity with the icosahedral ordering of the amorphous phase than the Al_3Zr_4 and CuZr_2 phases, which facilitates a lower interfacial energy and hence energy of formation for the $\text{Cu}_2\text{Zr}_4\text{O}$ phase.

4. Conclusions

The crystallization behaviour of suction cast and laser powder bed fusion processed AMZ4 ($\text{Zr}_{59.3}\text{Cu}_{28.8}\text{Al}_{10.4}\text{Nb}_{1.5}$ (at%)) at low temperatures were investigated using small angle neutron scattering, X-ray diffraction and scanning electron microscopy. The following observations are made:

- Electron microscopy and X-ray diffraction analysis of the annealed samples revealed a dense population of nanocrystals. The main phases were identified as CuZr_2 and Al_3Zr_4 in both materials.
- In-situ scattering measurements during annealing show that the crystallization occur at different characteristic length-scales in the cast material and the material processed by laser powder bed fusion.
- Fitting of the scattering data to a spherical particle model reveals a higher number density of particles and smaller average particle size in the LPBF processed material.
- The differences in the crystallization behaviour are attributed to the increased oxygen content of the LPBF processed material, which reduces the energy barrier to nucleation.

Our findings quantitatively demonstrates the role of oxygen in enhancing the phase separation rate in a Zr-based BMG. In terms of the LPBF process, unwanted oxygen dissolution can arise from both the powder atomization and the laser processing, in our study the latter played an important role. The oxygen content significantly reduces the thermal stability of the material and accelerates the crystallization process. Based on these observations, we anticipate that improved control of the oxygen dissolution in these processes would permit a broader selection of LPBF process parameters that are viable for fabrication of dense and amorphous components.

Data availability

The neutron scattering data are available at [58].

CRediT authorship contribution statement

A. Ericsson: Data curation, Formal analysis, Investigation, Methodology, Software, Validation, Visualization, Writing – original draft. **V. Pacheco:** Conceptualization, Data curation, Formal analysis, Investigation, Resources, Validation, Writing – review & editing. **J.J.**

Marattukalam: Data curation, Formal analysis, Investigation, Resources, Validation, Writing – review & editing. **R.M. Dalgliesh:** Data curation, Investigation, Methodology, Resources, Writing – review & editing. **A.R. Rennie:** Conceptualization, Funding acquisition, Investigation, Methodology, Supervision, Writing – review & editing. **M. Fisk:** Funding acquisition, Methodology, Resources, Software, Supervision, Writing – review & editing. **M. Sahlberg:** Conceptualization, Funding acquisition, Investigation, Project administration, Resources, Supervision, Writing – review & editing.

Declaration of Competing Interest

The authors declare the following financial interests/personal relationships which may be considered as potential competing interests: Anders Ericsson, Victor Pacheco, Jithin J. Marattukalam, Adrian R. Rennie and Martin Sahlberg have filed patent applications related to the use of Zr-based glass as a low-scattering material.

Acknowledgements

This work was carried out with financial support from the Swedish Foundation for Strategic Research (SSF), through the project Additive Manufacturing - Development of Process and Material [grant number GMT14-0048]; the strategic innovation program LIGHTer provided by Vinnova, Sweden's Innovation Agency [grant number 2020-04526]; and from the Swedish Foundation for Strategic Research (SSF) within the Swedish national graduate school in neutron scattering (SwedNess) [grant number GSn15-0008], which are gratefully acknowledged. Beamtime access to Larmor was provided using RB1910389 by STFC [58]. Victor Pacheco would like to thank Ashok Menon for his assistance with the Pawley refinements. The authors wish to thank Moritz Stolpe and Heraeus Additive Manufacturing GmbH for providing the cast samples and the powder feedstock material.

Supplementary material

Supplementary material associated with this article can be found, in the online version, at doi:[10.1016/j.jnoncrysol.2021.120891](https://doi.org/10.1016/j.jnoncrysol.2021.120891).

References

- [1] A. Suryanarayana, A. Inoue, *Bulk Metallic Glasses*, first ed., CRC Press, Boca Raton, FL, 2011.
- [2] M.F. Ashby, A.L. Greer, Metallic glasses as structural materials, *Scr. Mater.* 54 (3) (2006) 321–326, <https://doi.org/10.1016/j.scriptamat.2005.09.051>.
- [3] H. Liu, Q. Jiang, J. Huo, Y. Zhang, W. Yang, X. Li, Crystallization in additive manufacturing of metallic glasses: a review, *Addit. Manuf.* 36 (2020) 101568, <https://doi.org/10.1016/j.addma.2020.101568>.
- [4] A. Ericsson, V. Pacheco, M. Sahlberg, J. Lindwall, H. Hallberg, M. Fisk, Transient nucleation in selective laser melting of Zr-based bulk metallic glass, *Mater. Des.* 195 (2020) 108958, <https://doi.org/10.1016/j.matdes.2020.108958>.
- [5] Z. Mahbooba, L. Thorsson, M. Unosson, P. Skoglund, H. West, T. Horn, C. Rock, E. Vogli, O. Harrysson, Additive manufacturing of an iron-based bulk metallic glass larger than the critical casting thickness, *Appl. Mater. Today* 11 (2018) 264–269, <https://doi.org/10.1016/j.apmt.2018.02.011>.
- [6] P. Bordeenithikasek, M. Stolpe, A. Elsen, D.C. Hofmann, Glass forming ability, flexural strength, and wear properties of additively manufactured Zr-based bulk metallic glasses produced through laser powder bed fusion, *Addit. Manuf.* 21 (2018) 312–317, <https://doi.org/10.1016/j.addma.2018.03.023>.
- [7] X.P. Li, C.W. Kang, H. Huang, L.C. Zhang, T.B. Sercombe, Selective laser melting of an $\text{Al}_{88}\text{Ni}_6\text{Y}_{4.5}\text{Co}_{2}\text{La}_{1.5}$ metallic glass: processing, microstructure evolution and mechanical properties, *Mater. Sci. Eng. A* 606 (2014) 370–379, <https://doi.org/10.1016/j.msea.2014.03.097>.
- [8] L. Deng, S. Wang, P. Wang, U. Kühn, S. Pauly, Selective laser melting of a Ti-based bulk metallic glass, *Mater. Lett.* 212 (2018) 346–349, <https://doi.org/10.1016/j.matlet.2017.10.130>.
- [9] J.J. Marattukalam, V. Pacheco, D. Karlsson, L. Riekehr, J. Lindwall, F. Forsberg, U. Jansson, M. Sahlberg, B. Hjörvarsson, Development of process parameters for selective laser melting of a Zr-based bulk metallic glass, *Addit. Manuf.* 33 (2020) 101124, <https://doi.org/10.1016/j.addma.2020.101124>.
- [10] X.P. Li, M.P. Roberts, S. O'Keeffe, T.B. Sercombe, Selective laser melting of Zr-based bulk metallic glasses: processing, microstructure and mechanical properties, *Mater. Des.* 112 (2016) 217–226, <https://doi.org/10.1016/j.matdes.2016.09.071>.
- [11] S. Pauly, C. Schricker, S. Scudino, L. Deng, U. Kühn, Processing a glass-forming Zr-based alloy by selective laser melting, *Mater. Des.* 135 (2017) 133–141, <https://doi.org/10.1016/j.matdes.2017.08.070>.
- [12] J.P. Best, Z. Evenson, F. Yang, A.-C. Dippel, M. Stolpe, O. Gutowski, M.T. Hasib, X. Li, J.J. Kruzic, Structural periodicity in laser additive manufactured Zr-based bulk metallic glass, *Appl. Phys. Lett.* 115 (3) (2019) 031902, <https://doi.org/10.1063/1.5100050>.
- [13] J.P. Best, H.E. Ostergaard, B. Li, M. Stolpe, F. Yang, K. Nomoto, M.T. Hasib, O. Muránsky, R. Busch, X. Li, J.J. Kruzic, Fracture and fatigue behaviour of a laser additive manufactured Zr-based bulk metallic glass, *Addit. Manuf.* 36 (2020) 101416, <https://doi.org/10.1016/j.addma.2020.101416>.
- [14] V. Pacheco, D. Karlsson, J.J. Marattukalam, M. Stolpe, B. Hjörvarsson, U. Jansson, M. Sahlberg, Thermal stability and crystallization of a Zr-based metallic glass produced by suction casting and selective laser melting, *J. Alloys Compd.* 825 (2020) 153995, <https://doi.org/10.1016/j.jallcom.2020.153995>.
- [15] L. Deng, K. Kosiba, R. Limbach, L. Wondraczek, U. Kühn, S. Pauly, Plastic deformation of a Zr-based bulk metallic glass fabricated by selective laser melting, *J. Mater. Sci. Technol.* 60 (2021) 139–146, <https://doi.org/10.1016/j.jmst.2020.06.007>.
- [16] X. Lin, W. Johnson, W. Rhim, Effect of oxygen impurity on crystallization of an undercooled bulk glass forming Zr-Ti-Cu-Ni-Al Alloy, *Mater. Trans.* 38 (5) (1997) 473–477, <https://doi.org/10.2320/matertrans1989.38.473>.
- [17] I. Jonas, W. Hembree, F. Yang, R. Busch, A. Meyer, Industrial grade versus scientific pure: influence on melt properties, *Appl. Phys. Lett.* 112 (17) (2018) 1–5, <https://doi.org/10.1063/1.5021764>.
- [18] U. Köster, J. Meinhardt, S. Roos, R. Busch, Formation of quasicrystals in bulk glass forming Zr-Cu-Ni-Al alloys, *Mater. Sci. Eng. A* 226–228 (1997) 995–998, [https://doi.org/10.1016/S0921-5093\(97\)80100-1](https://doi.org/10.1016/S0921-5093(97)80100-1).
- [19] B.S. Murty, D.H. Ping, K. Hono, A. Inoue, Direct evidence for oxygen stabilization of icosahedral phase during crystallization of $\text{Zr}_{65}\text{Cu}_{27.5}\text{Al}_{7.5}$ metallic glass, *Appl. Phys. Lett.* 76 (1) (2000) 55–57, <https://doi.org/10.1063/1.125654>.
- [20] M.F. de Oliveira, W.J. Botta F., M.J. Kaufman, C.S. Kiminami, Phases formed during crystallization of $\text{Zr}_{55}\text{Al}_{10}\text{Ni}_5\text{Cu}_{30}$ metallic glass containing oxygen, *J. Non-Cryst. Solids* 304 (1–3) (2002) 51–55, [https://doi.org/10.1016/S0022-3093\(02\)01003-7](https://doi.org/10.1016/S0022-3093(02)01003-7).
- [21] J. Eckert, N. Mattern, M. Zinkevitch, M. Seidel, Crystallization behavior and phase formation in Zr-Al-Cu-Ni metallic glass containing oxygen, *Mater. Trans.* 39 (6) (1998) 623–632, <https://doi.org/10.2320/matertrans1989.39.623>.
- [22] J. Wegner, M. Frey, S. Kleszczynski, R. Busch, G. Witt, Influence of process gas during powder bed fusion with laser beam of Zr-based bulk metallic glasses, *Procedia CIRP* 94 (2020) 205–210, <https://doi.org/10.1016/j.procir.2020.09.039>.
- [23] J. Heinrich, R. Busch, B. Nonnenmacher, Processing of a bulk metallic glass forming alloy based on industrial grade Zr, *Intermetallics* 25 (2012) 1–4, <https://doi.org/10.1016/j.intermet.2012.02.011>.
- [24] Heraeus AMLOY Technologies, Material datasheet: AMLOY-ZR01, https://www.heraeus.com/media/media/group/media_group/products/amorphous_metals/Datasheet_AMLOY-ZR01_1.pdf.
- [25] R. Haynes, A.M. Paradowska, M.A. Chowdhury, C.M. Goodway, R. Done, O. Kirichek, E.C. Oliver, An inert-gas furnace for neutron scattering measurements of internal stresses in engineering materials, *Meas. Sci. Technol.* 23 (4) (2012), <https://doi.org/10.1088/0957-0233/23/4/047002>.
- [26] O. Arnold, J.C. Bilheux, J.M. Borreguero, A. Buts, S.I. Campbell, L. Chapon, M. Doucet, N. Draper, R. Ferraz Leal, M.A. Gigg, V.E. Lynch, A. Markvardsen, D. J. Mikkelsen, R.L. Mikkelsen, R. Miller, K. Palmen, P. Parker, G. Passos, T. G. Perring, P.F. Peterson, S. Ren, M.A. Reuter, A.T. Savici, J.W. Taylor, R.J. Taylor, R. Tolchenov, W. Zhou, J. Zikovsky, Mantid - Data analysis and visualization package for neutron scattering and μ SR experiments, *Nucl. Instrum. Methods Phys. Res. A* 764 (2014) 156–166, <https://doi.org/10.1016/j.nima.2014.07.029>.
- [27] R.K. Heenan, J. Penfold, S.M. King, SANS at pulsed neutron sources: present and future prospects, *J. Appl. Crystallogr.* 30 (1997) 1140–1147, <https://doi.org/10.1107/S0021889897002173>.
- [28] C. Zhou, C. Guo, C. Li, Z. Du, Thermodynamic assessment of the phase equilibria and prediction of glass-forming ability of the Al-Cu-Zr system, *J. Non-Cryst. Solids* 461 (2017) 47–60, <https://doi.org/10.1016/j.jnoncrysol.2016.09.031>.
- [29] N. Sohrabi, J. Jhabvala, G. Kurtuldu, M. Stoica, A. Parrilli, S. Berns, E. Polatidis, S. Van Petegem, S. Hugon, A. Neels, J.F. Löffler, R.E. Logé, Characterization, mechanical properties and dimensional accuracy of a Zr-based bulk metallic glass manufactured via laser powder-bed fusion, *Mater. Des.* 199 (2021), <https://doi.org/10.1016/j.matdes.2020.109400>.
- [30] C.F. Holder, R.E. Schaak, Tutorial on powder X-ray diffraction for characterizing nanoscale materials, *ACS Nano* 13 (7) (2019) 7359–7365, <https://doi.org/10.1021/acsnano.9b05157>.
- [31] C.T. Liu, M.F. Chisholm, M.K. Miller, Oxygen impurity and microalloying effect in a Zr-based bulk metallic glass alloy, *Intermetallics* 10 (11–12) (2002) 1105–1112, [https://doi.org/10.1016/S0966-9795\(02\)00131-0](https://doi.org/10.1016/S0966-9795(02)00131-0).
- [32] D. Ouyang, N. Li, L. Liu, Structural heterogeneity in 3D printed Zr-based bulk metallic glass by selective laser melting, *J. Alloys Compd.* 740 (2018) 603–609, <https://doi.org/10.1016/j.jallcom.2018.01.037>.
- [33] J.G. Barker, D.F. Mildner, Survey of background scattering from materials found in small-angle neutron scattering, *J. Appl. Crystallogr.* 48 (5) (2015) 1055–1071, <https://doi.org/10.1107/S1600576715010729>.
- [34] J.F. Löffler, W.L. Johnson, Model for decomposition and crystallization of Zr-based bulk amorphous alloys near the glass transition, *Mater. Sci. Eng. A* 304–306 (1–2) (2001) 670–673, [https://doi.org/10.1016/S0921-5093\(00\)01561-6](https://doi.org/10.1016/S0921-5093(00)01561-6).

- [35] E. Pekarskaya, J.F. Löffler, W.L. Johnson, Microstructural studies of crystallization of a Zr-based bulk metallic glass, *Acta Mater.* 51 (14) (2003) 4045–4057, [https://doi.org/10.1016/S1359-6454\(03\)00225-8](https://doi.org/10.1016/S1359-6454(03)00225-8).
- [36] X.L. Wang, J. Almer, C.T. Liu, Y.D. Wang, J.K. Zhao, A.D. Stoica, D.R. Haefner, W. H. Wang, In situ synchrotron study of phase transformation behaviors in bulk metallic glass by simultaneous diffraction and small angle scattering, *Phys. Rev. Lett.* 91 (26) (2003) 24–27, <https://doi.org/10.1103/PhysRevLett.91.265501>.
- [37] I. Martin, T. Ohkubo, M. Ohnuma, B. Deconihout, K. Hono, Nanocrystallization of $Zr_{41.2}Ti_{13.8}Cu_{12.5}Ni_{10.0}Be_{22.5}$ metallic glass, *Acta Mater.* 52 (15) (2004) 4427–4435, <https://doi.org/10.1016/j.actamat.2004.05.038>.
- [38] K. Kajiwara, M. Ohnuma, T. Ohkubo, D.H. Ping, K. Hono, APFIM/TEM/SAXS studies of early stage crystallization of a $Zr_{52.5}Cu_{17.9}Ni_{14.6}Al_{10}Ti_5$ metallic glass, *Mater. Sci. Eng. A* 375–377 (2004) 738–743, <https://doi.org/10.1016/j.msea.2003.10.087>.
- [39] X. Wu, S. Lan, X. Wei, J. Zhou, Z. Lu, J.D. Almer, X.L. Wang, Elucidating the nature of crystallization kinetics in $Zr_{46}Cu_{46}Al_8$ metallic glass through simultaneous WAXS/SAXS measurements, *Appl. Phys. Lett.* 114 (21) (2019) 211903, <https://doi.org/10.1063/1.5088984>.
- [40] G. Banfi, V. Degiorgio, A.R. Rennie, J.G. Barker, Small-angle neutron scattering study of crystal growth in semiconductor-doped glasses, *Phys. Rev. Lett.* 69 (23) (1992) 3401–3404, <https://doi.org/10.1103/PhysRevLett.69.3401>.
- [41] A. Debski, R. Debski, W. Gasior, New features of Entall database: comparison of experimental and model formation Enthalpies, *Arch. Metall. Mater.* 59 (4) (2014) 1337–1343, <https://doi.org/10.2478/amm-2014-0228>.
- [42] D.H. Kim, W.T. Kim, E.S. Park, N. Mattern, J. Eckert, Phase separation in metallic glasses, *Prog. Mater. Sci.* 58 (8) (2013) 1103–1172, <https://doi.org/10.1016/j.pmatsci.2013.04.002>.
- [43] S. Haas, J. Andersson, M. Fisk, J.S. Park, U. Lienert, Correlation of precipitate evolution with Vickers hardness in Haynes® 282® superalloy: in-situ high-energy SAXS/WAXS investigation, *Mater. Sci. Eng. A* 711 (2018) 250–258, <https://doi.org/10.1016/j.msea.2017.11.035>.
- [44] V.F. Sears, Neutron scattering lengths and cross sections, *Neutron News* 3 (3) (1992) 26–37, <https://doi.org/10.1080/10448639208218770>.
- [45] P. Villars, K. Cenzual, Pearson's Crystal Data: Crystal Structure Database for Inorganic Compounds (on DVD), Release 2020/2021, ASM International®, Materials Park, Ohio, USA.
- [46] R.B. Bergmann, A. Bill, On the origin of logarithmic-normal distributions: an analytical derivation, and its application to nucleation and growth processes, *J. Crystal Growth* 310 (13) (2008) 3135–3138, <https://doi.org/10.1016/j.jcrysgro.2008.03.034>.
- [47] D.W. Schaefer, R.K. Brow, B.J. Olivier, T. Rieker, G. Beauchage, L. Hrubesh, J.S. Lin, Characterization of Porosity in Ceramic Materials by Small-Angle Scattering: Vycor™ Glass and Silica Aerogel, in: H. Brumberger (Ed.), *Modern Aspects of Small-Angle Scattering*, Springer Netherlands, Dordrecht, 1995, pp. 299–307, https://doi.org/10.1007/978-94-015-8457-9_10.
- [48] J.S. Pedersen, Determination of size distributions from small-angle scattering data for systems with effective hard-sphere interactions, *J. Appl. Crystallogr.* 27 (1994) 595–608, <https://doi.org/10.1107/S0021889893013810>.
- [49] N.W. Ashcroft, J. Lekner, Structure and resistivity of liquid metals, *Phys. Rev.* 145 (1) (1966) 83–90, <https://doi.org/10.1103/PhysRev.145.83>.
- [50] K.F. Kelton, Liquid structure and long range diffusion: their impact on glass formation and nanoscale devitrification, *Intermetallics* 14 (8–9) (2006) 966–971, <https://doi.org/10.1016/j.intermet.2006.01.014>.
- [51] L. Yang, M.K. Miller, X.L. Wang, C.T. Liu, A.D. Stoica, D. Ma, J. Almer, D. Shi, Nanoscale solute partitioning in bulk metallic glasses, *Adv. Mater.* 21 (3) (2009) 305–308, <https://doi.org/10.1002/adma.200801183>.
- [52] J. Schroers, Processing of bulk metallic glass, *Adv. Mater.* 22 (14) (2010) 1566–1597, <https://doi.org/10.1002/adma.200902776>.
- [53] K.F. Kelton, A. Greer, *Nucleation in Condensed Matter: Applications in Materials and Biology*, first ed., Pergamon, Oxford, 2010.
- [54] J. Russo, H. Tanaka, The microscopic pathway to crystallization in supercooled liquids, *Sci. Rep.* 2 (2012) 505, <https://doi.org/10.1038/srep00505>.
- [55] C. Fan, X. Yue, A. Inoue, C.T. Liu, X. Shen, P.K. Liaw, Recent topics on the structure and crystallization of Al-based glassy alloys, *Mater. Res.* 22 (1) (2019) 1–15, <https://doi.org/10.1590/1980-5373-MR-2018-0619>.
- [56] Z. Altounian, E. Batalla, J.O. Strom-Olsen, J.L. Walter, The influence of oxygen and other impurities on the crystallization of $NiZr_2$ and related metallic glasses, *J. Appl. Phys.* 61 (1) (1987) 149–155, <https://doi.org/10.1063/1.338847>.
- [57] K. Momma, F. Izumi, VESTA 3 for three-dimensional visualization of crystal, volumetric and morphology data, *J. Appl. Crystallogr.* (2011), <https://doi.org/10.1107/S0021889811038970>.
- [58] M. Sahlberg, A.R. Rennie, V. Pacheco, R.M. Dalgliesh, A. Ericsson, J. Marattukalam, In-situ Devitrification of a Zr-based Metallic Glass $Zr_{59.3}Cu_{28.8}Al_{10.4}Nb_{1.5}$ Produced by Suction Casting and 3D Printing, STFC ISIS Facility, 2019, <https://doi.org/10.5286/ISIS.E.RB1910389>.